CARDIFF UNIVERSITY
PRIFYSGOL CAERDYDD

ORCA – Online Research @ Cardiff

This is an Open Access document downloaded from ORCA, Cardiff University's institutional repository:https://orca.cardiff.ac.uk/id/eprint/162013/

This is the author's version of a work that was submitted to / accepted for publication.

Citation for final published version:

Kim, Ji-Yeop, Jin, Mi-Jin, Hou, Bo , Kim, Minsoo P., Um, Doo-Seung and Kim, Chang-Il 2023. Reducing the oxygen vacancy concentration in SrTiO3-δ thin films via an optimized O2 plasma treatment for enhancing device properties. Applied Surface Science 639 , 158271. 10.1016/j.apsusc.2023.158271

Publishers page: http://dx.doi.org/10.1016/j.apsusc.2023.158271

Please note:
Changes made as a result of publishing processes such as copy-editing, formatting and page numbers may not be reflected in this version. For the definitive version of this publication, please refer to the published source. You are advised to consult the publisher's version if you wish to cite this paper.

This version is being made available in accordance with publisher policies. See http://orca.cf.ac.uk/policies.html for usage policies. Copyright and moral rights for publications made available in ORCA are retained by the copyright holders.

Reducing the Oxygen Vacancy Concentration in $SrTiO_{3-\delta}$ Thin Films via an Optimized O_2 Plasma Treatment for Enhancing Device Properties

Ji-Yeop Kim[1,2], Mi-Jin Jin[2], Bo Hou[3], Minsoo P. Kim[4], Doo-Seung Um[5,*], Chang-Il Kim[1,*]

[1]School of Electrical and Electronics Engineering, Chung-Ang University, Seoul 06974, Republic of Korea

[2]Center for Multidimensional Carbon Materials (CMCM), Institute for Basic Science (IBS), Ulsan 44919, Republic of Korea

[3]School of Physics and Astronomy, Cardiff University, Cardiff CF24 3AA, United Kingdom

[4] Department of Chemical Engineering, Sunchon National University, Suncheon 57922, Republic of Korea

[5]Department of Electrical Engineering, Sejong University, Seoul 05006, Republic of Korea

*Correspondence: dsum@sejong.ac.kr (D.-S.U.); cikim@cau.ac.kr (C.-I.K.)

Keywords: oxygen vacancy, defect control, $SrTiO_3$, sputtered thin film, plasma treatment, dielectric material

Abstract

Perovskite materials, specifically strontium titanate ($SrTiO_3$, STO) thin films, have gained significant attention in materials science and electronics owing to their unique properties. However, low-temperature fabrication via sputtering can introduce oxygen vacancies that compromise film quality. O_2 plasma treatment (OPT) has the potential to improve film properties, such as bond recomposition, electrical conductivity, and optical properties, by reducing the number of oxygen vacancies. In this study, STO films treated by O_2 plasma were characterized using analytical techniques to understand the OPT-induced microstructural, morphological, and optical changes in these films. In addition, the possibility of improving device properties by low-temperature processes was confirmed by exploring the correlation between the number of oxygen vacancies reduced by the OPT process and the enhanced film properties. This result is expected to promote the application of STO thin films in flexible electronic devices and display components and provides insights into the role of oxygen vacancies and the effectiveness of OPT as a low-temperature solution for reducing their number.

Graphical abstract

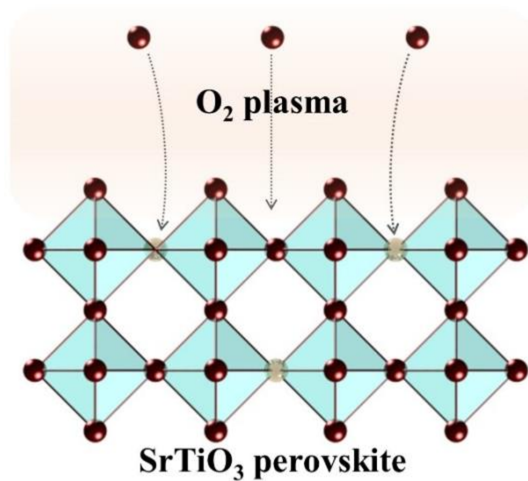

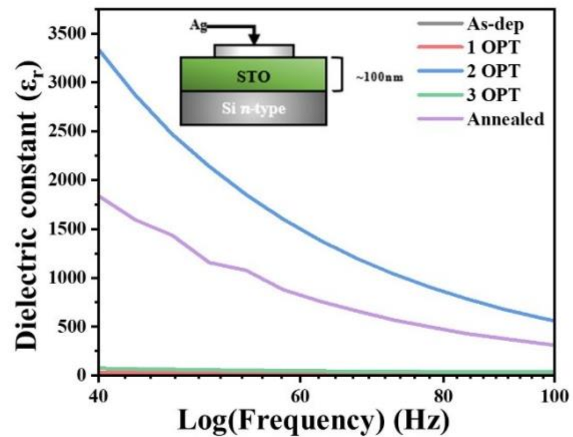

Highlights

- Reduction of oxygen vacancy concentration in $SrTiO_3$ thin films by O_2 plasma treatment
- Defect control through a low-temperature process
- Changes in band gap and work function of SrTiO3 thin films by oxygen plasma treatment
- $SrTiO_3$-based capacitor with an improved dielectric constant in the low-frequency region

Introduction

Perovskite materials, such as strontium titanate ($SrTiO_3$, STO) thin films[1], have garnered significant attention in the fields of materials science and electronics because of their unique and diverse properties, including ferroelectricity[2, 3], magnetism, and electrical[4] and optical characteristics. These properties stem from the flexible crystallographic structure of perovskites, which allows the incorporation of various metal or organic cations (A and B sites) and anions (X site)[5]. The crystal structures of various ABX_3 perovskite oxides can be distinguished as functions of their tolerance factor (t) with references to an ideal cubic structure (Figure 1(a)). For example, STO thin films, a typical perovskite material with a tolerance factor[6] close to 1[7, 8], exhibit several attractive features, such as a high dielectric constant[9, 10], a low electrical loss[11], and optical transparency[12].

STO thin films have been widely employed as building blocks in electronic components, such as high-frequency filters, capacitors, and transistors, as well as in various optical devices

like lenses, polarizers, and reflective and transmissive coatings. However, low-temperature fabrication via sputtering can compromise the quality of the resulting thin films[13, 14], primarily due to the presence of oxygen vacancies.

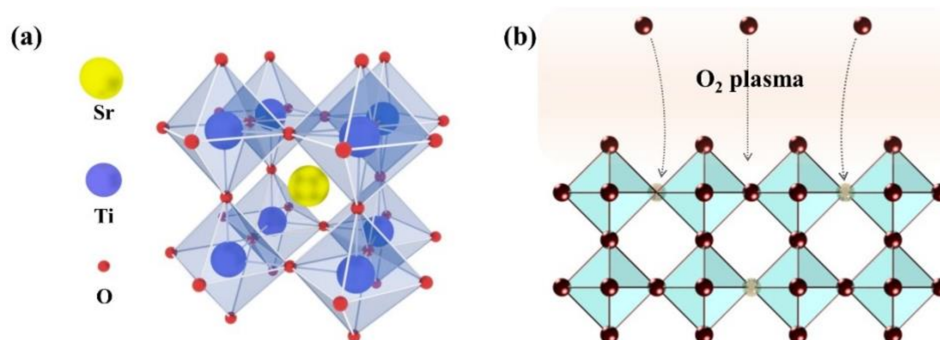

Fig. 1. Schematics of a perovskite crystal structure and OPT. (a) Perovskite crystal structure, (b) The mechanism for filling oxygen vacancies with oxygen ions in the plasma.

The presence of defects such as anion (X site) or cation (A and B sites) vacancies in perovskite structure can influence material characteristics. In particular, these vacancies could trap the charge carrier, alter local bonding configurations, and subsequently modify the polarization and dielectric constant of the STO films. Therefore, several techniques such as high-temperature annealing and high-pressure treatments in the presence of hydrogen, oxygen, or nitrogen have been used to enhance film quality by minimizing the number of oxygen vacancies[15]. Nevertheless, these high-temperature annealing processes are unsuitable for flexible electronic devices because of their adverse effects on the mechanical properties and overall integrity of the devices. Hence, a low-temperature process that can effectively control or reduce the number of oxygen vacancies in thin films needs to be developed for manufacturing thin-film-based flexible electronics and display devices.

Several methods[16], each with its own set of advantages and limitations, have been previously proposed to regulate oxygen vacancies in STO thin films. Although traditional methods, such as annealing and ion implantation, specifically with Ar and O[17, 18] ions, can effectively control the number of oxygen vacancies generated, they require high-temperature processing[19], which is incompatible with the requirements of flexible electronics. Alternative approaches, such as atomic layer deposition (ALD) and chemical vapor deposition, enable better control over film properties. However, these methods may still require elevated temperatures during processing, and the ALD process, in particular, can be less favorable because of its low throughput and high costs[20]. The sputtering deposition method suits specific goals such as flexible and display devices processing due to its advantages of a relatively simple setup, low-temperature process, and high versatility. Although sputtering has the advantages of a low deposition temperature and high deposition rate compared to ALD, it generates a large number of defects, such as oxygen vacancies[21]. Given the limitations of the existing methods, it is essential to develop a low-temperature process for controlling the number of oxygen vacancies in STO thin films to enhance their applicability in flexible electronic devices and

display components. One promising approach for addressing this issue is the application of O_2 plasma treatment (OPT), a process that exploits high-energy oxygen ions and atoms to control surface and bulk defects in materials such as Figure 1(b). This technique involves the use of reactive oxygen plasma generated by an ionizing oxygen gas in a high-power density electromagnetic field.

The active oxygen ions in the plasma react with the surface of the film and thus reduce the number of oxygen vacancies or improve the surface properties. These high-energy oxygen ions physically collide with the surface of the STO film and fill the generated oxygen vacancies, resulting in surface rearrangement or recomposition, which help in reducing the defect density and enhancing the structural stability of the film[22]. Furthermore, active oxygen ions and atoms chemically react with the STO film, thereby reducing the number of oxygen vacancies. Consequently, OPT injects oxygen ions into vacancy sites and thus decreases the defect density as well as improves the electrical[23-25], optical[26], and mechanical properties of the film.

In this study, we investigated the effects of OPT on the properties of STO thin films by assessing the feasibility to control and minimize the oxygen vacancy concentration in such films and by evaluating the resulting improved performances of the electronic and optical devices. We systematically evaluated the impact of various OPT parameters and characterized the treated films using a range of analytical techniques to obtain insights into the microstructural, morphological, and optical changes induced by the OPT. We comprehensively explored the correlation between the reduced oxygen vacancy concentration and the enhanced properties of the films. The results are expected to contribute to the development of an optimized low-temperature process for controlling the concentration of oxygen vacancies in STO thin films. This study is expected to pave the way for the widespread application of these materials in flexible electronic devices and display components as well as provide valuable insights into the role of oxygen vacancies in STO thin films and the effectiveness of OPT as a viable alternative low-temperature method for reducing oxygen vacancy concentration.

Experiment Method

In this study, STO thin films were deposited on Si (100) substrates (N-type (As), 500–550 μm, < 0.005 Ω-cm) by radiofrequency (RF) magnetron sputtering. A 1/8-inch-thick $SrTiO_3$ target (99.95 %, TASCO, USA) with a diameter of 2 inches and Cu bonded to a backplate, was utilized. Prior to the sputtering, $15 \times 15\, mm^2$ silicon and quartz glass substrates were ultrasonically cleaned in isopropyl alcohol, rinsed with deionized water, and finally dried using N_2 gas. To minimize contamination, the chamber's base pressure was maintained at 5×10^{-5} Torr for one hour using an oil diffusion pump.

The STO thin films were deposited on Si and quartz glass wafers for 1 h under the following conditions: a substrate temperature of 27 °C, an RF power of 40 W, an operating pressure of 2.7 mTorr, an Ar flow rate of 30 sccm, and a substrate-to-target distance of 15 cm. The surface was hydrophilized by ultraviolet (UV) light (253.7 nm) treatment, before the deposition, to improve adhesion of the surface to the Si and quartz glass. This step was essential to prevent the formation of voids between the STO thin film and electrodes for obtaining accurate capacitance values. The deposited STO thin film had a thickness of approximately 100–150 nm.

OPT was performed using a Planar High-Density Plasma (HDP; SELEX 200, APTC, South Korea) system, in which the upper RF antenna was operated at a frequency of 13.56 MHz; this antenna integrated both the plate structure of the capacitively coupled plasma sources and the coil structure of the inductively coupled plasma sources for plasma generation and density control. The lower RF generator operated at a frequency of 2 MHz and controlled the ion energy and radical motion energy within the plasma. Before the OPT, the chamber's base pressure was maintained at 5×10^{-6} Torr for 30 min using a turbo molecular pump. The wafer chuck was connected to a cooling system to maintain a constant substrate temperature of 27 °C during the OPT.

The plasma conditions for the OPT process were optimized with upper and lower RF powers of 500 and 150 W, respectively. Each OPT process was performed for 5 minutes, with a 10-minute cooling time provided every 1 minute to prevent overheating. In this experiment, the labels 1 OPT, 2 OPT, and 3 OPT refer to the number of times the OPT was applied, with all conditions remaining consistent for each application. To verify the effect of OPT, as-deposited and annealed samples were prepared as a controlled group. The annealing process was carried out in an 800 °C furnace for 1 hour in an oxygen atmosphere, and the deposited STO thin film was characterized by X-ray diffraction (XRD) data (Figure S01).

This study investigated the changes in electrical properties of STO thin films as the oxygen vacancy concentration was controlled via OPT. Oxygen vacancies were indirectly identified through XPS, reflecting changes in the material's electronic states and atomic structure, as direct detection through photoelectron signals from missing oxygen atoms is not possible. First, X-ray photoelectron spectroscopy (XPS; NEXSA, ThermoFisher Scientific, USA) was used to verify the changes in the oxygen vacancy concentration, whereas UV-vis spectrophotometry (Lambda 35; PerkinElmer, USA) was used to measure the optical transmittance and observe the variations in the optical bandgap by the OPT process. Additionally, the changes in the work function and surface roughness of the films were investigated. The work function was measured by Kelvin probe force microscopy (KPFM) using an electrostatic force microscopy (EFM) tip (ElectriMulti75-G; Park Systems, South Korea), and the surface roughness was measured by atomic force microscopy (AFM; NX-10, Park Systems, South Korea). The surface structure of the thin films was observed using a field-emission scanning electron microscope (SEM; FE-SEM-2, SIGMA 300, Carl Zeiss, Germany) and analyzed by XRD (D8 DISCOVER, BRUKER, USA). Furthermore, the changes in the surface roughness and defect density due to the recomposition process were evaluated.

Based on these results, we evaluated the changes in the physical and electrical properties of the fabricated STO thin films by controlling the oxygen vacancy concentration through the OPT. After depositing a 140-nm-thick STO thin film, $3 \times 3\ mm^2$Ag (99.99 %) electrodes were deposited using a thermal evaporator (KVT-2004, KOREAVAC, South Korea) for measuring the capacitance. The electrical performances of the STO-based capacitors under various OPT conditions were analyzed using an impedance analyzer (4294A Agilent, Keysight, USA).

Results and discussion

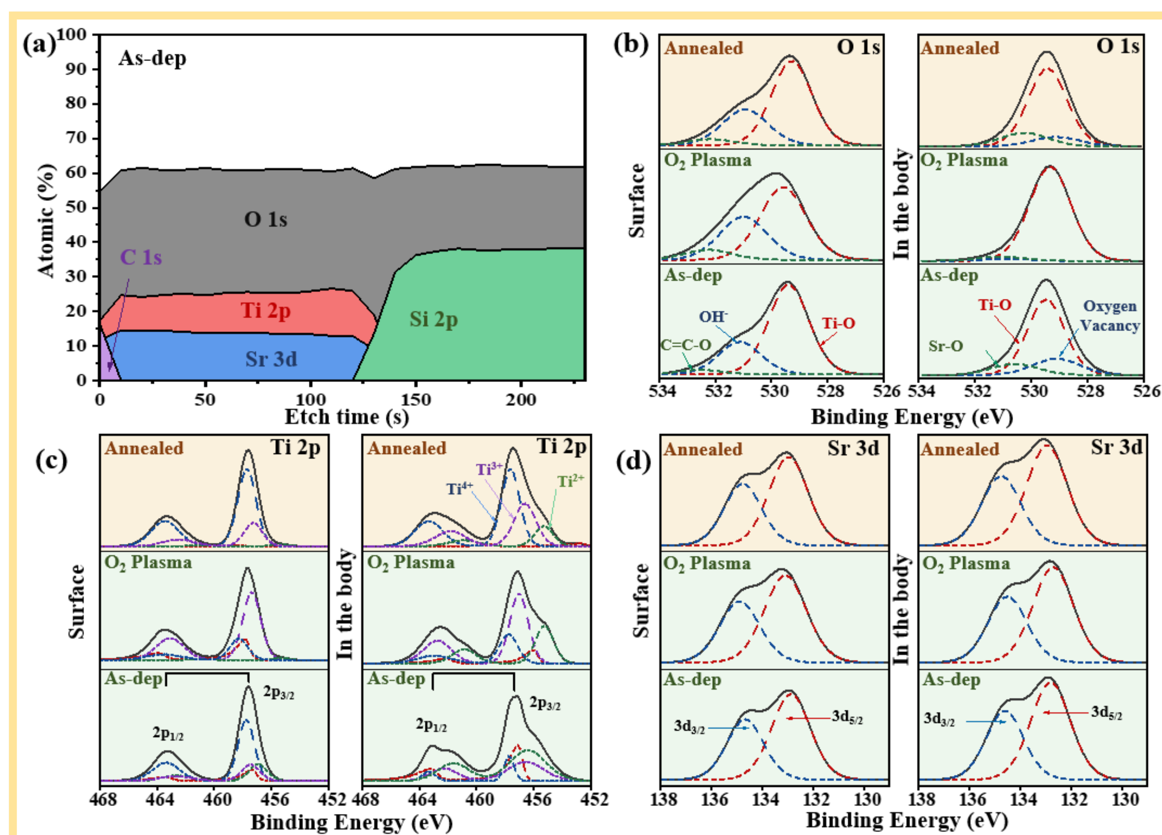

Fig. 2. XPS analysis of the STO films. (a) XPS depth profiles of the STO films, illustrating the atomic composition ratios as functions of etching time: O 1s (black), Ti 2p (red), Sr 3d (blue), Si 2p (green), and C 1s (purple). Deconvoluted graphs of (b) O 1s, (c) Ti 2p, and (d) Sr 3d for the as-deposited, O_2 plasma treated, and annealed STO films. The left side represents the XPS data obtained from the surface, while the right side displays XPS data obtained from the uncontaminated STO body.

Figure 2(a) displays the XPS depth profiles of the STO thin films, achieved via ion beam etching, and reveals the atomic ratios from the surface to approximately 140 nm deep within the as-deposited STO film. (graphs of the O_2-plasma-treated and annealed STO thin films are provided in Figure S02) The C 1s spectrum detected during the initial 0–15 s indicates the presence of a carbon contamination layer within the film. From 15 to 120 s, a pure STO film without other impurities is observed. The Si 2p peak observed after 120 s originates from quartz substrate (SiO_2). Hence, analysis is performed only up to the point before the quartz substrate

peak is visible. Figures 2 (b-d) compare the atomic ratios according to the binding energies of O 1s, Ti 2p, and Sr 3d for the contamination layer (surface) and pure STO layer (interior).

All the XPS spectra were deconvoluted using the CasaXPS (Version 2.3.24PR1.0, Casa Software Ltd) program with a Shirley-type baseline. For the deconvoluting the line-shapes of O 1s and Sr 3d, a Gaussian/Lorentzian (30) function was used, while an asymmetric Lorentzian function (1.1,5,7) was applied for deconvoluting the Ti(0) line-shape in the Ti 2p spectrum. The Ti 2p and Sr 3d peaks exhibit area ratios of 1:2 for "p" subshells[27] and 2:3 for "d" subshells[28, 29] due to spin–orbit splitting. Due to the inconsistencies in the exact binding-energy peak positions of the Ti(II) and Ti(III) oxides reported in previous studies, and the good agreement between the Ti $2p_{3/2}$ peak positions of Ti(IV) and Ti metal, we used the following energy intervals for Ti splitting: Ti(0) at 6.1 eV, Ti(IV) at 5.7 eV, Ti(III) at 5.2 eV, and Ti(II) at 5.6 eV[30-32]. Our initial fitting parameters for the Ti 2p spectra were developed using the averaged binding energy data and $2p_{1/2}$–$2p_{3/2}$ splitting data obtained from the NIST XPS database, which provided a reliable basis for our analysis. The interval between Sr $3d_{5/2}$ and $3d_{3/2}$ was set to 1.73 eV[33-35]. The XPS spectra were calibrated using the C 1s peak (284.84 eV) and adjusted considering the peaks of O 1s, Sr 3d, Ti 2p, and Si 2p. In Figure 2 (b), the red line with the largest binding ratio at the surface (O 1s) represents the Ti–O bond (= 529.4 eV)[36-38], the green line with the smallest binding ratio signifies the carbon bond, C=O–C (=532.3 eV)[39], and the blue line indicates hydrogen one, OH^- (= 531.0 eV)[40, 41]. Compared to the surface of the STO films, the interior exhibits an increase in the Ti–O bond, and a complete absence of OH^- bonds, highlighting the differences between the chemical environment at the surface and that in the interior regions of the STO films. This bond is most suitable for the perovskite structure of STO and matches the surface Ti–O bond energy. The O 1s peak at 528.8 eV indicates the presence of oxygen vacancies in the interior of the film material. Examining the ratios of each O 1s bond in Table 1, oxygen vacancies account for 19.08 % of the total O 1s in the as-deposited film, but decrease to 4.75 % after the OPT and 10.94 % after the annealing treatment. These results confirm that OPT is more effective in controlling oxygen vacancies. As seen in Figure S03, the annealed STO thin films demonstrate a significant reduction in the number of oxygen vacancies near the SiO_2 substrate (at depths of approximately 80–120 nm). This result can be attributed to oxygen diffusion from the SiO_2 substrate during the annealing process of the STO thin films.

We analyzed the Ti 2p and Sr 3d peaks visible in the spectra shown in Figures 2 (c) and (d) to assess the ability of the OPT process to control oxygen vacancies as well as reduce defect density. Figure 2 (c) shows the deconvoluted peaks from the Ti 2p peak into components corresponding to Ti^{4+} (blue line), Ti^{3+} (purple line), Ti^{2+} (green line), and Ti (0) (red line). As the state transitions to Ti^{2+}, Ti^{3+}, and Ti^{4+}, the number of bonds increases, resulting in an increase in binding energy. Consequently, the deconvolved Ti 2p peaks can be identified from left to right as Ti^{4+}, Ti^{3+}, and Ti^{2+}. The Ti^{2+} bonding peak on the surface of the STO thin film is considered due to defects of the thin film under the sputtering deposition process. The dominant ionic species on the surface and inside of the thin film show contrasting behaviors depending on the post-process. Specifically, on the surface, the Ti^{4+} ion dominated the binding ratio subsequent to the as-deposition and annealing, whereas the Ti^{3+} ion demonstrated the highest binding ratio after the OPT process. However, the inside of the annealed and O_2 plasma-treated STO thin film still maintains a constant ratio at a depth of more than 10 nm, while the inside of the as-deposited thin film shows significant changes such as the increases of Ti^{3+} and

Ti^{2+} ratios with drastic decreases of the Ti^{4+} ratio. This means that natural oxygen cannot deeply penetrate into the as-deposited thin film. On the other hand, the ratio of Ti^{4+} and Ti^{3+} increases after the OPT process, which means that the oxygen ions in plasma can reach deep into the film to reduce oxygen defects and generate Ti^{4+} and Ti^{3+} bonding. The strong increase in the ratio of Ti^{4+} and Ti^{3+} after the annealing process indicates that the oxidation process significantly enhances at high temperatures. This result suggests that the O_2 plasma under low temperature induces sufficient oxidation throughout the entire depth of the thin film although not as high-temperature annealing.

Inside the STO thin films, the binding ratio of Ti^{4+} significantly increases from 10.27 % after the OPT to 19.55 % and 50.79 % after the annealing. However, the degree of oxidation, as signified by the formation of Ti^{4+}, did not reach the level observed in the annealed STO, indicating a lower level of oxidation. Conversely, the binding ratio of Ti^{3+} greatly increases from 25.87 % in the as-deposited film to 46.80 % after the OPT and 33.59 % after the annealing. Lastly, the binding ratio of Ti^{2+} underwent a significant decrease from 41.58 % in the as-dep film to 26.23 % after the OPT and declined to 12.93% after the annealing. This result suggests an enhancement in the binding ratio transition from Ti^{3+} to Ti^{4+} as the oxidation process intensifies. Additionally, the decrease in the concentration of oxygen vacancies in the OPT, compared to the annealed, is speculated to be due to OPT inducing a uniform distribution of Ti^{3+} across the entire film. Consequently, while OPT may not provide a high degree of oxidation, it can sufficiently contribute to reducing oxygen vacancies by increasing the binding ratio up to Ti^{3+}. As such, our result suggests that the degree of oxidation to Ti^{3+} appears to be sufficient to minimize the ratio of oxygen vacancies in the STO thin film.

Moreover, the Sr 3d binding-energy peak shown in Figure 2 (d) is deconvoluted into Sr $3d_{3/2}$ and Sr $3d_{5/2}$. There is no difference between the Sr 3d peak originating from the surface and that arising from the interior, and these peaks do not change significantly after the OPT and annealing. This indicates that the oxygen vacancies are not affected by the Sr–O bond. These results demonstrate that the OPT effectively controls oxygen vacancies without inducing additional defects in STO thin films. Furthermore, the Ti–O bond (Ti^{4+}, Ti^{3+}, Ti^{2+}) is the primary cause of oxygen vacancy formation in as-deposited STO thin films, whereas the Sr–O bond does not produce any oxygen vacancy.

Sample		**Chemical composition (%)**		
		As-deposited	**O_2 plasma treated**	**Annealed**
	V_O	19.08	4.75	10.94
In the body	**Ti^{4+}**	10.27	19.55	50.79
	Ti^{3+}	25.87	46.80	33.59

Ti^{2+}	41.58	26.23	12.93

Table. 1. Chemical composition ratios of oxygen vacancies (V_O), Ti^{4+}, Ti^{3+}, and Ti^{2+} determined from the XPS profiles of the STO films. Left column indicates V_O, Ti^{4+}, Ti^{3+}, and Ti^{2+}, while the top row shows the as-deposited, OPT, and annealed conditions.

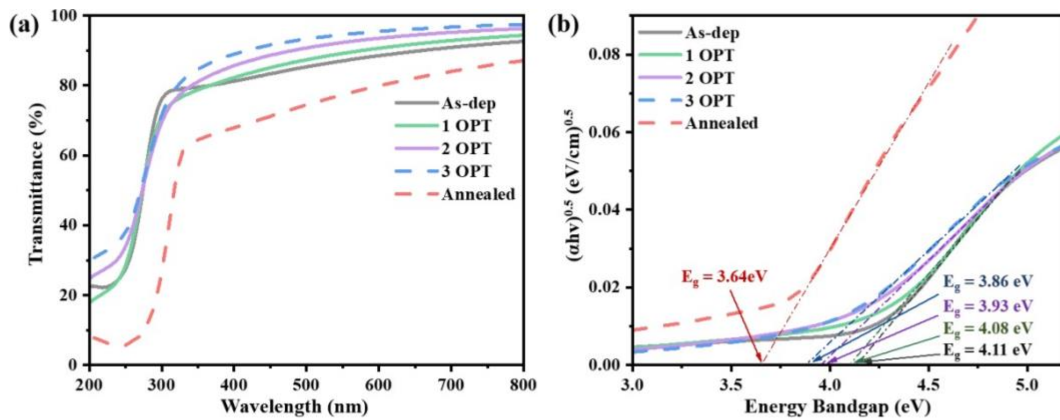

Fig. 3. Optical properties of the STO films. (a) Optical transmittance spectra of the as-deposited (black line), 1 OPT (green line), 2 OPT (purple line), 3 OPT (blue line), and annealed (red line; at 800 °C for 1 h) STO films. (b) Optical bandgap of the STO films.

The optical, electrical, and structural properties[42] of the films are significantly affected by their surface states, including chemical composition, oxygen (or cation) vacancy concentration[43], grain boundaries, and potential defects[44]. The presence of defects and impurities can result in light scattering, absorption, and optical inhomogeneity, while defects like oxygen (or cation) vacancies and impurities can act as charge carriers and alter the film's conductivity[45], carrier concentration, and mobility. Therefore, we additionally investigated the changes in the optical and electrical properties of the O_2-plasma-treated STO thin films. Figure 3 shows the transmittance and optical bandgap of a 140-nm-thick STO thin film[46], measured by UV-vis spectrophotometry. Figure 3(a) reveals that the transmittance of the STO thin film increases as the number of OPT increases. This result is considered to be due to the reduction of the film thickness and surface roughness due to the etching effect by the ion bombardment of the O_2 plasma under the DC bias. However, the annealing process increases the roughness of the surface during crystallization. (In this process, the change in film thickness is not significantly observed.) In particular, a significant number of voids occur between the grains of the STO film, which causes a decrease in transmittance due to light scattering[47, 48].

Figure 3(b) displays the optical bandgap calculated from the transmittance using the Tauc-plot formula (Equation 1).

$$\alpha h v = A(h v - E_g)^{\gamma} \tag{1}$$

where α represents the absorption coefficient, v denotes photon frequency, h is Planck's constant, A is a proportionality constant, E_g is the bandgap energy, and γ corresponds to the nature of the electronic transition. The value of γ depends on the bandgap of the film; $\gamma = 2$ and 1/2 for direct and indirect bandgap, respectively. Because the STO thin film exhibits indirect transitions, we used $\gamma = 1/2$ in the calculations[49, 50]. The Beer–Lambert law was used to determine the absorption coefficient (α) as follows (Equation 2)[51]:

$$\log\left(\frac{I}{I}\right) = \log\left(e^{-\alpha x}\right) \tag{2}$$

where I_0 denotes the intensity of the incident light, I represent the intensity of the transmitted light, and x (=1) is the depth of penetration.

Consequently, the calculated optical bandgap decreases progressively from 4.11 eV (as-deposited sample) to 4.08 eV (1 OPT sample), 3.93 eV (2 OPT sample), and 3.86 eV (3 OPT sample)[52]. The annealed crystalline STO thin film exhibits an optical bandgap of 3.64 eV. This reduction in bandgap is considered to be due to the changes in the film composition, such as changes in the concentration of oxygen vacancies and cationic vacancies[53].

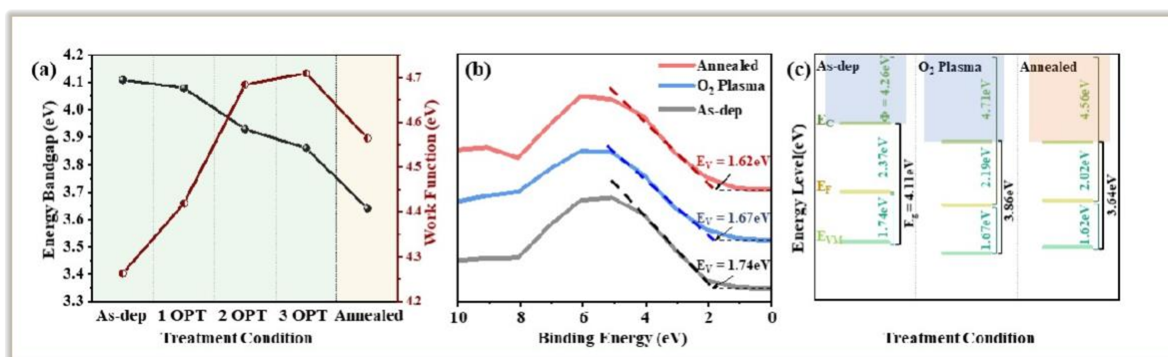

Fig. 4. Bandgap and work function relationship. (a) Graph showing STO's optical bandgap (black axis) and work function (red axis). (b) Maximum valence band measurements by XPS. (c) Band structure diagrams of the as-deposited, 1 OPT, 2 OPT, 3 OPT, and annealed STO films.

Figure 4(a) depicts the relationship between the work function and optical bandgap of the STO thin films. The work function was measured by KPFM using an AFM equipment and EFM tip. KPFM, which utilizes the EFM technique, is widely employed to analyze the local surface potential distribution or work function of a sample. The AFM cantilever applies an alternating voltage between the tip and the sample, and a direct current bias compensates for the potential difference between the tip and the sample. This method is employed to measure the sample surface potential as a feedback signal[54]. The measured work function is shown in

Figure S04, and the sample's potential is determined using Equation (3):

$$\phi_{\text{Sample}} = \phi_{\text{Tip}} - V_{\text{CPD}} \quad (3)$$

Here, Φ_{Sample} represents the work function of the sample, Φ_{Tip} is the work function of the tip, and V_{CPD} is the measured KPFM potential. An aluminum and gold reference sample (PFKPFM-SMPL; Bruker, USA) was used for calibrating the tip potential measurements. The work function of the STO thin film is 4.26 eV in its initial state, 4.41 eV in the 1 OPT state, 4.68 eV in the 2 OPT state, 4.71 eV in the 3 OPT state, and 4.56 eV in the annealed state. Consequently, as the number of OPTs increases, the work function increases from 4.26 eV to 4.71 eV, suggesting that the increase in the work function is related to the decrease in the oxygen vacancy concentration[55, 56], and surface carbon impurities[57, 58]. It's important to note that the valence band measurements by XPS reflect the distance from the Fermi level to the maximum valence band[60]. The initial energy of the maximum valence band value for the as-deposited state was measured at 1.74 eV. This value undergoes a significant change after OPT and annealing; the energy decreases to 1.67 eV after OPT and further to 1.62 eV after annealing. The distance from the Fermi level to the minimum conduction band depending on calculation from the measured optical bandgap and the valence band energy also decreases from the initial 2.37 eV in the as-deposited state to 2.19 eV after OPT, and to 2.02 eV after annealing. There is a reduction in the oxygen vacancy concentration as the number of OPTs increases, which leads to an increased work function and a concurrent decrease in the optical bandgap, maximum valence band energy, and minimum conduction band energy. This trend is likely due to a decrease in defect-related states in the STO thin films as a result of OPT and the annealing process. The reduction of defect-related states can change the physical, and chemical properties of STO thin films. In conclusion, the decrease in bandgap and energy distance for both the maximum valence band and minimum conduction band can be attributed to the decrease in defect-related states.

Sample	**Optical bandgap (eV)**	**Work function (eV)**	**E_F-E_{VMax} (eV)**
As-deposited	4.11	4.26	1.74
O_2 plasma treated	3.86	4.71	1.67
Annealed	3.64	4.56	1.62

Table. 2. Optical bandgap, work function, and valence band of the as-deposited, O_2-plasma-treated, and annealed (at 800 °C) STO thin films.

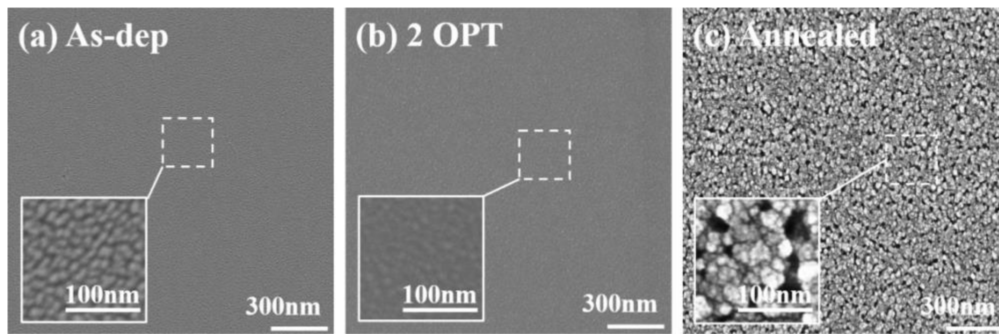

Fig. 5. SEM images of the STO films. (a) As-deposited state, (b) OPT process, and (c) as-deposited STO film annealed at 800 °C for 1 h.

Figure 5 displays the SEM images of the STO thin films. The large images are magnified 50,000 times, and the small images are magnified 200,000 times. For the SEM imaging of the thin films, a 3-nm-thick layer of Pt was deposited. Figure 5(a-c) show the images of as-deposited, O_2-plasma-treated, and annealed (at 800 °C) STO thin films, respectively. STO exhibits an amorphous state at room temperature, whereas after annealing at temperatures above 800 °C, the crystallinity of the thin film stabilizes[59]. The STO thin film annealed at 800 °C (Figure 5(c)) undergoes a crystallization process, transitioning from the amorphous state (a) to a crystalline state (c). During this crystallization process, volume shrinkage occurs, which leads to the formation of voids between the grain[60]. Although the proportion of oxygen vacancies in the annealed STO thin film decreases, the vacancies are not completely eliminated from the films. During the fabrication of oxide thin films, such defects can degrade the electrical and physical properties of the films. Interestingly, Figure 5(b) demonstrates that OPT can effectively control the concentration of oxygen vacancies without generating additional surface defects in thin films.

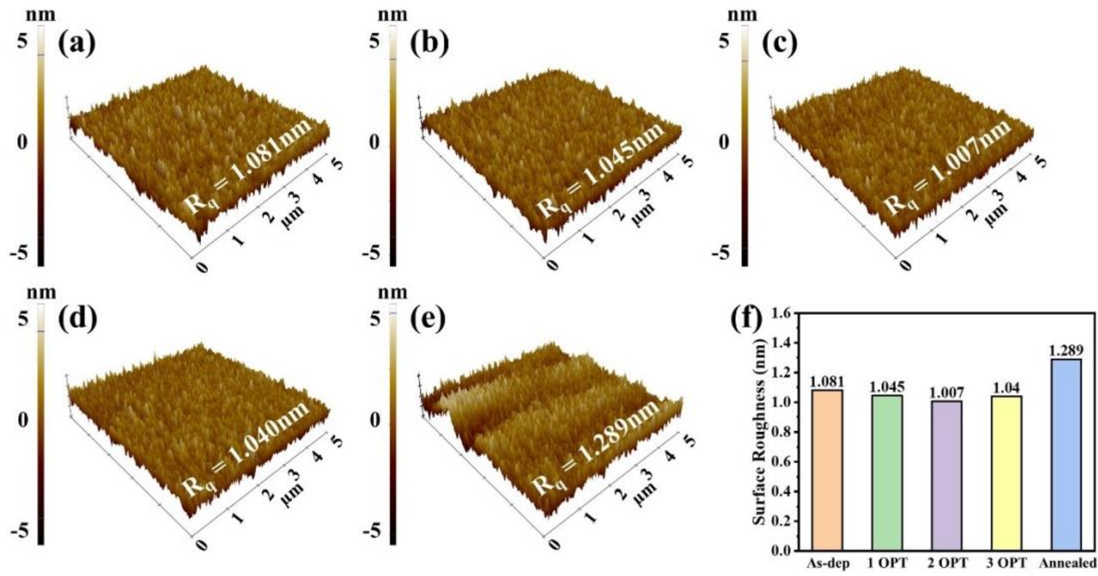

Fig. 6. AFM images of the STO films. (a) As-deposited state, (b)-(d) films subjected to repeated OPT, (e) as-deposited STO film annealed at 800 °C for 1 h, and (f) bar chart of surface roughness.

Figure 6 shows the surface roughness of the STO thin film measured by AFM after OPT and annealing and indicates the effect of controlling the oxygen vacancy concentration on the surface roughness of the STO thin film. While the as-deposited STO thin film exhibits a roughness (R_q) of 1.081 nm, the roughness (R_q) measured for the samples after 1, 2, and 3 OPT processes (Figure 6(b-d)) are 1.045, 1.007, and 1.040 nm, respectively. This result indicates that the surface roughness of STO film tends to decrease as the exposure time to the O_2 plasma increases.

The decrease in the roughness of the OPT samples is due to the adsorption of oxygen ions in the plasma onto oxygen vacancies on the surface. However, in the case of the 3 OPT sample, the oxygen vacancy concentration in the film is already saturated, which impedes the movement of the oxygen ions into the film's interior. The activated oxygen ions that are unable to penetrate the film contribute to the etching of the STO surface, or when the oxygen concentration becomes excessive, the lattice mismatch increases[61], which leads to an increase in the roughness of the STO layer.

Consequently, maximum oxygen saturation is expected between the 2 OPT and 3 OPT processes, whereby the surface roughness is considered to slightly increase in the 3 OPT process. Figure 6(e) displays an annealed STO thin film with a roughness (R_q) of 1.289 nm, which is more than 20 % higher than that of the as-deposited film. The SEM image in Figure 5(c) reveals that the increased surface roughness can be attributed to the increase in crystallinity and surface void growth.

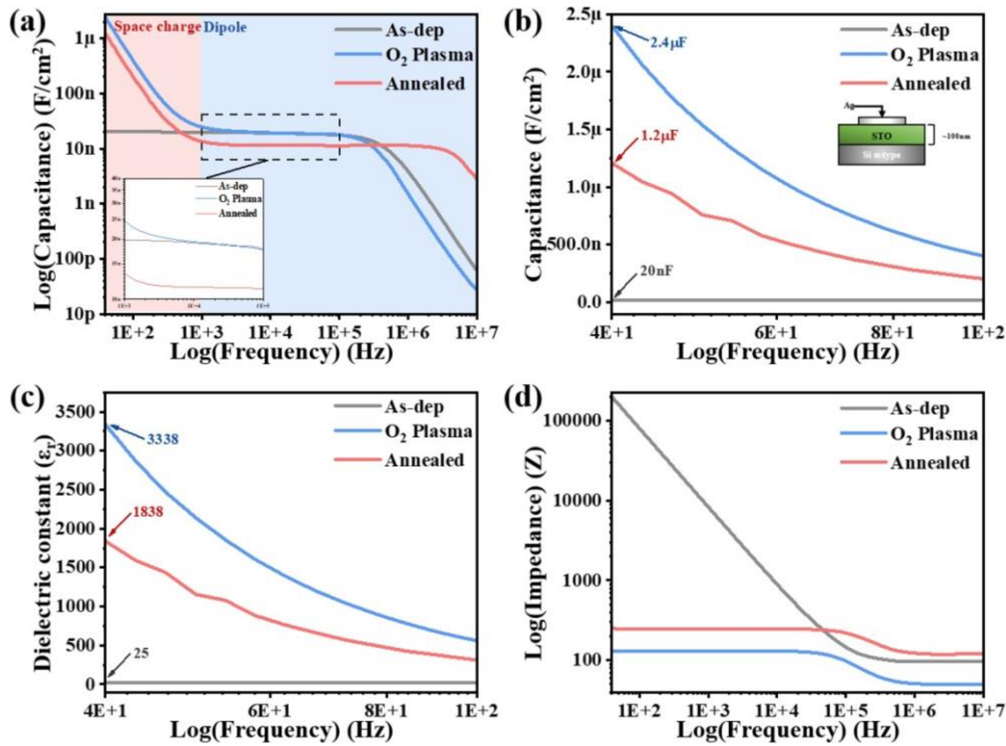

Fig. 7. Capacitance measurements of the STO films using an impedance analyzer. (a) Logarithmic capacitance, (b) linear capacitance, (c) dielectric constant, and (d) impedance of the as-deposited (black line), O_2-plasma-treated (blue line), and annealed (red line) STO films.

To examine the changes in the electrical properties of the films due to the reduction in the oxygen vacancy concentration, STO was deposited on a highly doped n-type Si wafer by RF sputtering. The capacitance and impedance of the films were measured in the frequency range of 40 to 10^7 Hz using an impedance analyzer (Figure 7). The device's structure can be confirmed from the schematic shown in the inset in Figure 7(b). After depositing a 140-nm-thick STO thin film, $3 \times 3\ mm^2$ Ag electrodes were deposited using a thermal evaporator. Figure 7(a) presents the capacitance spectra, which reveal the occurrence of dielectric polarization that is typically observed in dielectric materials[62]. Results for as-deposited and 1-3 OPT samples can be found in Figure S05. Dielectric polarization categorically spans four distinct frequency ranges: electronic polarization ($>10^{15}$ Hz), ionic polarization (10^7–10^{12} Hz), dipole polarization (10^3–10^7 Hz), and space charge (or interfacial) polarization ($<10^3$ Hz)[63-65]. Polarizability of dielectric materials weakens in the presence of oxygen vacancies, because these vacancies are electrically neutral and thus respond slowly to changes in dielectric materials. However, as the number of oxygen vacancies decreases, they become electrically active, and the dielectric polarizability of the material enhances, which in turn increases the capacitance of the material. Figures 7(a) and (b) show the capacitance expressed in logarithmic and linear scales, respectively. The black, red, and blue lines represent the capacitance spectra of the as-deposited, annealed STO, and O_2-plasma-treated STO films, respectively. The dissipation factor for these films can be inspected in Figure S06. The capacitance detected

below 1000 Hz is caused by space charge polarization, and this result confirms that annealing or OPT affects the space charges present in dielectric materials[66]. Therefore, the increase in the capacitance of the STO films after the OPT and annealing can be attributed to the reduction in the number of oxygen vacancies. The capacitances of the as-deposited and annealed STO films are 20 nF and 1.2 μF at 40 Hz, respectively, whereas that of the O_2-plasma-treated STO increases to 2.4 μF, which is twice that of the annealed STO.

From 1000 Hz to 10^7 Hz, dipole polarization occurs. All the three samples show a constant polarization value in this frequency band; however, compared to the as-deposited sample, the annealed one shows a decrease in capacitance magnitude, and the frequency range of its dipole polarization expands as well. In contrast, after the OPT, the capacitance magnitude changes only negligibly, whereas the frequency range of dipole polarization slightly decreases. The decrease in capacitance with increasing frequency can be ascribed to the rapid changes in electron movement, which disrupt the alignment of the dipoles within a dielectric material, thereby suppressing charge accumulation[67]. Figure 7(c) shows the dielectric constant determined from the measured capacitance, thin film thickness, and electrode area using the following equation 4:

$$\mathbf{C} = \varepsilon_{\mathbf{r}} * \varepsilon_{\mathbf{0}} \frac{\mathbf{A}}{\mathbf{d}} \qquad (4)$$

where C represents capacitance, ε_r represents the relative permittivity of the dielectric, ε_0 represents the permittivity of vacuum, d represents the thickness of the dielectric, and A represents the electrode area. At a frequency of 40 Hz, the calculated dielectric constant of the as-deposited STO capacitor is 25, which amplifies to 1838 for the annealed STO capacitor, and further elevates to 3338 for the O_2-plasma-treated STO capacitor. Thus, both the dielectric constant and capacitance of the STO capacitor increase as the oxygen vacancy concentration decreases within the dielectric material. Figure 7(d) shows the impedance of all the fabricated and treated STO capacitors. Compared to the as-deposited STO capacitor, both the annealed and O_2-plasma-treated STO capacitors demonstrate a significant decrease in impedance. In particular, the impedance of the O_2-plasma-treated STO capacitor is lower than that of the recrystallized STO capacitor, suggesting a higher electrical stability.

In summary, the electrical properties of STO thin films were investigated, with a focus on the reduction of oxygen vacancy concentration. The capacitance and dielectric constant increased as the number of oxygen vacancies reduced within the dielectric materials. Furthermore, both the annealed and the O_2-plasma-treated STO capacitors showed lower impedances and improved stability compared to the as-deposited STO capacitor. These results provide valuable insights into the electrical properties of STO thin films and reveal the influence of oxygen vacancies on dielectric polarization and capacitance of dielectric materials.

Conclusions

In this study, we evaluated the changes in the physical and electrical properties of STO thin films by controlling the oxygen vacancy concentration via OPT. XPS analysis showed that the oxygen vacancy concentration of the STO thin film decreased from 19.08 % to 4.11 % after

the OPT treatment. Further, the optical bandgap of the STO thin film decreased up to 3.86 eV upon the OPT. Moreover, the surface roughness of the STO film subjected to OPT also decreased, and the optimal surface roughness (R_q) was 1.007 nm. These results demonstrate that controlling the oxygen vacancy concentration in STO films via OPT is an effective and efficient strategy to reduce the surface defect density as well as minimize the adverse effects of oxygen vacancies on these films. Furthermore, the changes in the physical properties of the STO films subjected to OPT can be evaluated by comparing the measured properties with those of an annealed STO film. We observed that the capacitance increased, and the electrical stability improved in the STO thin films subjected to OPT. These results demonstrate that the electrical properties of STO thin films can be improved by controlling the concentration of oxygen vacancies via OPT.

CRediT authorship contribution statement

Ji-Yeop Kim: Conceptualization, Validation, Investigation, Data Curation, Visualization, Writing - original draft. **Mi-Jin Jin:** Conceptualization, Methodology, Investigation, Resources. **Bo Hou:** Methodology, Investigation, Writing - Review & Editing. **Minsoo P. Kim:** Investigation, Resources, Writing - Review & Editing. **Doo-Seung Um:** Conceptualization, Methodology, Resources, Visualization, Writing - Review & Editing, Supervision. **Chang-Il Kim:** Conceptualization, Writing - Review & Editing, Supervision, Project administration, Funding acquisition.

Acknowledgments

This research was supported by the Chung-Ang University Research Grants in 2021, the National Research Foundation (NRF) of Korea (2021M3H4A1A02050421) and the Institute for Basic Science (IBS-R019-Y1)

Conflict of interest

The authors declare that they have no conflict of interests.

Appendix A. Supplementary material

Supplementary data to this article can be found online at https://

Reference

1. Fujimoto, K., Y. Kobayashi, and K. Kubota, *Growth of BaTiO3□ SrTiO3 thin films by rf magnetron sputtering.* Thin Solid Films, 1989. **169**(2): p. 249-256.

2. Scott, J., *Applications of modern ferroelectrics.* science, 2007. **315**(5814): p. 954-959.

3. Lee, D., et al., *Emergence of room-temperature ferroelectricity at reduced dimensions.* Science, 2015. **349**(6254): p. 1314-1317.

4. Mude, N.N., et al., *Highly stable, solution-processed Ga-doped IZTO thin film transistor by Ar/O2 plasma treatment.* Advanced Electronic Materials, 2019. **5**(12): p. 1900768.

5. Ji, Q., et al., *The role of oxygen vacancies of ABO 3 perovskite oxides in the oxygen reduction reaction.* Energy & Environmental Science, 2020. **13**(5): p. 1408-1428.

6. Park, N.-G., *Perovskite solar cells: an emerging photovoltaic technology.* Materials today, 2015. **18**(2): p. 65-72.

7. Qiao, H.W., et al., *A gradient heterostructure based on tolerance factor in high-performance perovskite solar cells with 0.84 fill factor.* Advanced Materials, 2019. **31**(5): p. 1804217.

8. Li, Z., et al., *Stabilizing perovskite structures by tuning tolerance factor: formation of formamidinium and cesium lead iodide solid-state alloys.* Chemistry of Materials, 2016. **28**(1): p. 284-292.

9. Robertson, J., *High dielectric constant oxides.* The European Physical Journal-Applied Physics, 2004. **28**(3): p. 265-291.

10. Iwabuchi, M. and T. Kobayashi, *Growth and characterization of epitaxial SrTiO3 thin films with prominent polarizability.* Journal of applied physics, 1994. **75**(10): p. 5295-5301.

11. Popovici, M., et al., *Low leakage Ru-strontium titanate-Ru metal-insulator-metal capacitors for sub-20 nm technology node in dynamic random access memory.* Applied Physics Letters, 2014. **104**(8): p. 082908.

12. Liu, J., et al., *Visible and infrared transparency in lead-free bulk BaTiO3 and SrTiO3 nanoceramics.* Nanotechnology, 2010. **21**(7): p. 075706.

13. Abdullah, S., et al., *Influence of substrate annealing on inducing Ti3+ and oxygen vacancy in TiO2 thin films deposited via RF magnetron sputtering.* Applied Surface Science, 2018. **462**: p. 575-582.

14. Dong, H., et al., *Phase selectivity of ternary Zn-O-Sn films regulated by oxygen and fluorine.* Materials Today Communications, 2023. **35**: p. 105486.

15. Wang, H., et al., *Recrystallization behavior, oxygen vacancy and photoluminescence performance of sputter-deposited Ga2O3 films via high-vacuum in situ annealing.* Ceramics International, 2022. **48**(3): p. 3481-3488.

16. Rata, A.D., et al., *Defect-induced magnetism in homoepitaxial SrTiO3.* APL materials, 2022. **10**(9): p. 091108.

17. Zheng, X., *The influence of ion implantation-induced oxygen vacancy on electrical conductivity of WO3 thin films.* Vacuum, 2019. **165**: p. 46-50.

18. Xiao, X., et al., *Greatly reduced leakage current in BiFeO3 thin film by oxygen ion implantation.* Journal of Physics D: Applied Physics, 2007. **40**(18): p. 5775.

19. Yang, Z., et al., *Epitaxial SrTiO3 films with dielectric constants exceeding 25,000.* Proceedings of the

National Academy of Sciences, 2022. **119**(23): p. e2202189119.

20. Olsen, T., et al., *Co-sputtering yttrium into hafnium oxide thin films to produce ferroelectric properties.* Applied Physics Letters, 2012. **101**(8): p. 082905.

21. Kim, K., et al., *Ferroelectricity in undoped-HfO 2 thin films induced by deposition temperature control during atomic layer deposition.* Journal of Materials Chemistry C, 2016. **4**(28): p. 6864-6872.

22. Hiramatsu, T., et al., *Correlation between crystallinity and oxygen vacancy formation in In–Ga–Zn oxide.* Japanese Journal of Applied Physics, 2016. **55**(2): p. 021203.

23. Ren, Y., et al., *Study of oxygen plasma treatment on solution-processed SnO x thin-film transistors.* Journal of Physics D: Applied Physics, 2022. **55**(32): p. 325102.

24. Lim, K.H., et al., *UV–visible spectroscopic analysis of electrical properties in alkali metal-doped amorphous zinc tin oxide thin-film transistors.* Advanced Materials, 2013. **25**(21): p. 2994-3000.

25. Han, J., et al., *Reduction in interface trap density of Al2O3/SiGe gate stack by electron cyclotron resonance plasma post-nitridation.* Applied Physics Express, 2013. **6**(5): p. 051302.

26. Pinto, F., et al., *Oxygen defects and surface chemistry of reducible oxides.* Frontiers in Materials, 2019. **6**: p. 260.

27. Biesinger, M.C., et al. *Quantitative chemical state XPS analysis of first row transition metals, oxides and hydroxides*. in *Journal of Physics: Conference Series*. 2008. IOP Publishing.

28. Pauly, N., et al., *XPS primary excitation spectra of Zn 2 p, Fe 2 p, and Ce 3 d from ZnO, α-Fe2O3, and CeO2.* Surface and interface analysis, 2019. **51**(3): p. 353-360.

29. Scofield, J.H., *Hartree-Slater subshell photoionization cross-sections at 1254 and 1487 eV.* Journal of Electron Spectroscopy and Related Phenomena, 1976. **8**(2): p. 129-137.

30. González-Elipe, A., et al., *Compositional changes induced by 3.5 keV Ar+ ion bombardment in Ni-Ti oxide systems: A comparative study.* Surface Science, 1989. **220**(2-3): p. 368-380.

31. Pouilleau, J., et al., *Structure and composition of passive titanium oxide films.* Materials Science and Engineering: B, 1997. **47**(3): p. 235-243.

32. Biesinger, M.C., et al., *Resolving surface chemical states in XPS analysis of first row transition metals, oxides and hydroxides: Sc, Ti, V, Cu and Zn.* Applied surface science, 2010. **257**(3): p. 887-898.

33. Pilleux, M.E., C.R. Grahmann, and V.M. Fuenzalida, *Hydrothermal strontium titanate films on titanium: an XPS and AES depth-profiling study.* Journal of the American Ceramic Society, 1994. **77**(6): p. 1601-1604.

34. Vasquez, R., *X-ray photoelectron spectroscopy study of Sr and Ba compounds.* Journal of Electron Spectroscopy and Related Phenomena, 1991. **56**(3): p. 217-240.

35. Vasquez, R.P., *SrTiO3 by XPS.* Surface Science Spectra, 1992. **1**(1): p. 129-135.

36. Takagi-Kawai, M., et al., *The adsorption and the reaction of NH3 and NO x on supported V2O5 catalysts: effect of supporting materials.* Canadian Journal of Chemistry, 1980. **58**(20): p. 2132-2137.

37. Leinen, D., et al., *Ion beam induced chemical vapor deposition procedure for the preparation of oxide thin films. II. Preparation and characterization of Al x Ti y O z thin films.* Journal of Vacuum Science & Technology A: Vacuum, Surfaces, and Films, 1996. **14**(5): p. 2842-2848.

38. Sleigh, C., et al., *On the determination of atomic charge via ESCA including application to organometallics.* Journal of electron spectroscopy and related phenomena, 1996. **77**(1): p. 41-57.

39. Beamson, G. and D. Briggs, *High resolution XPS of organic polymers.* 1992: Wiley.

40. McIntyre, N., et al., *Chemical information from XPS—applications to the analysis of electrode surfaces.* Journal of Vacuum Science and Technology, 1981. **18**(3): p. 714-721.

41. Lorenz, P., et al., *ESCA investigations of some NiO/SiO2 and NiO—Al2 O3/SiO2 catalysts.* Journal of Electron Spectroscopy and Related Phenomena, 1979. **16**(3): p. 267-276.

42. Chen, C., et al., *Controllable defect driven symmetry change and domain structure evolution in BiFeO 3 with enhanced tetragonality.* Nanoscale, 2019. **11**(17): p. 8110-8118.

43. Ye, J., et al., *Defect passivation in lead-halide perovskite nanocrystals and thin films: toward efficient LEDs and solar cells.* Angewandte Chemie, 2021. **133**(40): p. 21804-21828.

44. Li, W., et al., *Defects in complex oxide thin films for electronics and energy applications: challenges and opportunities.* Materials Horizons, 2020. **7**(11): p. 2832-2859.

45. Garcia-Barriocanal, J., et al., *Colossal ionic conductivity at interfaces of epitaxial ZrO2: Y2O3/SrTiO3 heterostructures.* Science, 2008. **321**(5889): p. 676-680.

46. Kan, D., et al., *K. U, Y. Shimakawa and M. Takano.* Nature Materials, 2005. **4**: p. 816.

47. Yu, H., et al., *Essential role of oxygen vacancy in electrochromic performance and stability for WO3-y films induced by atmosphere annealing.* Electrochimica Acta, 2020. **332**: p. 135504.

48. Jia, T., et al., *The influence of oxygen vacancy on the electronic and optical properties of ABO 3− δ (A= La, Sr, B= Fe, Co) perovskites.* Physical Chemistry Chemical Physics, 2019. **21**(36): p. 20454-20462.

49. Wang, Y., et al., *Modulating the electronic and optical properties for SrTiO3/LaAlO3 bilayers treated as the 2D materials by biaxial strains.* Journal of Physics: Condensed Matter, 2020. **32**(21): p. 215701.

50. Batool, A., et al., *The pressure-induced indirect to direct bandgap transition and thermoelectric response in SrTiO3: An ab-initio study.* Journal of Physics and Chemistry of Solids, 2018. **123**: p. 70-75.

51. Mayerhöfer, T.G., S. Pahlow, and J. Popp, *The bouguer-beer-Lambert law: Shining light on the obscure.*

ChemPhysChem, 2020. **21**(18): p. 2029-2046.

52. Vu, T.K.O., D.U. Lee, and E.K. Kim, *The effect of oxygen partial pressure on band gap modulation of Ga2O3 grown by pulsed laser deposition.* Journal of Alloys and Compounds, 2019. **806**: p. 874-880.

53. Chen, D., et al., *Preferential cation vacancies in perovskite hydroxide for the oxygen evolution reaction.* Angewandte Chemie International Edition, 2018. **57**(28): p. 8691-8696.

54. Zhang, H., et al., *Torsional Harmonic Kelvin Probe Force Microscopy for High-Sensitivity Mapping of Surface Potential.* IEEE Transactions on Industrial Electronics, 2021. **69**(2): p. 1654-1662.

55. Li, Z., et al., *AZO work function enhanced by oxygen plasma immersion ion implantation.* Vacuum, 2023. **212**: p. 112038.

56. Liu, C., et al., *Enhanced photocatalytic degradation performance of BiVO4/BiOBr through combining Fermi level alteration and oxygen defect engineering.* Chemical Engineering Journal, 2022. **449**: p. 137757.

57. Yu, Y., D. Lee, and B. Jeong, *The dependence of the work function of Pt (1 1 1) on surface carbon investigated with near ambient pressure X-ray photoelectron spectroscopy.* Applied Surface Science, 2023. **607**: p. 155005.

58. Kuo, F.-L., et al., *Workfunction tuning of zinc oxide films by argon sputtering and oxygen plasma: an experimental and computational study.* Journal of Physics D: Applied Physics, 2012. **45**(6): p. 065301.

59. Ma, J., et al., *Optical properties of SrTiO 3 thin films deposited by radio-frequency magnetron sputtering at various substrate temperatures.* Journal of Applied Physics, 2006. **99**(3): p. 033515.

60. Xu, K., et al., *Effect of crystallization on the band structure and photoelectric property of SrTiO3 sol–gel derived thin film.* Journal of Alloys and Compounds, 2015. **653**: p. 7-13.

61. Wang, L., et al., *Improvement of the conductivity and transmittance of AZO/Ag/AZO composite film via lattice oxygen ratio regulation.* Optical Materials, 2021. **122**: p. 111672.

62. El Khaled, D., et al., *Dielectric spectroscopy in biomaterials: Agrophysics.* Materials, 2016. **9**(5): p. 310.

63. Liu, T., et al., *Microporous Co@ CoO nanoparticles with superior microwave absorption properties.* Nanoscale, 2014. **6**(4): p. 2447-2454.

64. Koops, C., *On the dispersion of resistivity and dielectric constant of some semiconductors at audiofrequencies.* Physical review, 1951. **83**(1): p. 121.

65. George, M., et al., *Finite size effects on the electrical properties of sol–gel synthesized CoFe2O4 powders: deviation from Maxwell–Wagner theory and evidence of surface polarization effects.* Journal of Physics D: Applied Physics, 2007. **40**(6): p. 1593.

66. Liu, Y., et al., *Oxygen vacancy-induced dielectric polarization prevails in the electromagnetic wave-absorbing mechanism for Mn-based MOFs-derived composites.* Advanced Functional Materials,

2022. **32**(34): p. 2204499.

67. Acharya, T. and R. Choudhary, *Structural, dielectric and impedance characteristics of CoTiO3.* Materials Chemistry and Physics, 2016. **177**: p. 131-139.